Available online at www.sciencedirect.com
ScienceDirect
Fluid Phase Equilibria 261 (2007) 396–406
FLUID PHASE EQUILIBRIA
www.elsevier.com/locate/fluid

Direct measurements of multi-component hydrates on the seafloor: Pathways to growth

K.C. Hester [a,1], R.M. Dunk [b,2], P.M. Walz [b], E.T. Peltzer [b], E.D. Sloan [a], P.G. Brewer [b,*]

[a] *Center for Hydrate Research, Colorado School of Mines, Golden, CO 80401, USA*
[b] *Monterey Bay Aquarium Research Institute, 7700 Sandholdt Road, Moss Landing, CA 95039, USA*

Received 11 May 2007; received in revised form 9 July 2007; accepted 9 July 2007
Available online 3 August 2007

Abstract

The phase behavior of multi-component hydrate systems formed in the ocean has been studied using a sea-going *in situ* Raman spectrometer. Results from a field study using a synthetic hydrate sample and preliminary measurements of naturally occurring thermogenic hydrates at Barkley Canyon are reported and compared. This work follows early field trials using simple and binary synthetic hydrates and an expedition to Hydrate Ridge, studying natural hydrates primarily composed of methane. This refined Raman technique was combined with visual observations utilizing remotely operated vehicles as experimental platforms in an oceanic laboratory. Traditional laboratory Raman analysis was also performed on hydrate samples following recovery.

A synthetic hydrate was first studied in Monterey Bay to characterize the formation, evolution, and dissociation of multi-component gas hydrates formed in the deep ocean as a guide to understanding complex behavior of natural hydrate systems. The gas mixture (92.5% CH_4, 3.8% C_2H_6, 1.9% C_3H_8, 0.4% *i*-C_4H_{10}, 0.4% *n*-C_4H_{10}, 0.1% *i*-C_5H_{12}, 0.1% *n*-C_5H_{12}, and 0.1% neo-C_5H_{12}) was chosen to simulate a typical natural gas composition. Regions of sII and mixed sI–sII hydrate were measured *in situ* after 65 days of formation. The presence of a heterogeneous inter-mixed sI–sII hydrate suggests a formation mechanism where hydrate growth proceeds from localized pockets of isolated gas, such as gas bubbles separated from the bulk vapor phase by hydrate membranes, where sI formation follows the depletion of sII-forming gases within these individual hydrate reactors. Unstable conditions during recovery led to significant hydrate dissociation, leaving only ice and a compositionally homogenous sII hydrate phase, with no evidence of the sI that had been observed at the seafloor.

To investigate whether this process may operate in natural systems, a Raman investigation of the natural thermogenic hydrates at Barkley Canyon was carried out. Massive seafloor hydrate outcrops varied in appearance from yellow, due to oil staining, to white. While the yellow hydrate had significant interference due to fluorescence, detailed analysis of the *in situ* Raman data was possible for the white hydrate. This white hydrate was mainly sII, but the presence of sI was also detected. The heterogeneity in both structure and composition of these natural hydrates was similar to the synthetic hydrate formed in Monterey Bay. These similarities suggest that a controlled seafloor experiment was able to simulate a natural thermogenic hydrate with reasonable accuracy. Further development of theory and testing is needed to determine if the 'individual hydrate reactor' mechanism was indeed the pathway to growth in this natural system.

Keywords: *In situ*; Raman spectroscopy; Gas hydrates; Thermogenic

1. Introduction

Gas hydrates are non-stoichiometric crystalline solids formed when water is combined with non-associating low molecular weight "guest" molecules [1]. Stability conditions depend on the hydrate guests but low temperatures and high pressures are typically required. Three hydrate structures are commonly observed: structure I (sI), structure II (sII), and structure H (sH).

For simple hydrates (one guest type and water), guest size generally determines the stable structure. The sI lattice forms with molecules in the size range of 4.2–6 Å, such as methane and ethane. Two cage types are present in the sI crystal lattice: six $5^{12}6^2$ cages/unit cell and two 5^{12} cages/unit cell. The sII lattice forms with molecules less than 4.2 Å, such as argon, and between 6 and 7 Å, such as propane. Two cage types are also

* Corresponding author. Tel.: +1 831 775 1706; fax: +1 831 775 1620.
E-mail address: brpe@mbari.org (P.G. Brewer).
[1] Present address: Monterey Bay Aquarium Research Institute, 7700 Sandholdt Road, Moss Landing, CA 95039, USA.
[2] Present address: Department of Chemistry, University of York, Heslington, York YO10 SDD, UK.

0378-3812/$ – see front matter © 2007 Elsevier B.V. All rights reserved.
doi:10.1016/j.fluid.2007.07.053

present in the sII crystal lattice: eight $5^{12}6^4$ cages/unit cell and sixteen 5^{12} cages/unit cell. The sH lattice (except at very high pressures) requires two guests to form: one large guest between 7 and 9 Å, such as *i*-pentane, and one smaller guest such as methane. This hydrate has three cage types: one $5^{12}6^8$ cage/unit cell, two $4^35^66^3$ cages/unit cell, and three 5^{12} cages/unit cell. More complex behavior is observed in multi-guest hydrate systems. For example a methane + ethane mixture (both form sI hydrates as single gases) can form either sI or sII depending on composition and *P*, *T* conditions [2].

The low temperature and high pressure conditions needed for hydrate formation are present in most of the world's oceans. While the pressure and temperature conditions may be adequate, hydrate only forms when guest molecules are present in sufficient concentrations such as in gas accumulations in continental shelf sediments [3]. Current estimates of hydrate reserves ($2.5–440 \times 10^{15}$ m^3 of methane at STP [4,5]) have led to work exploring hydrates as a future energy source. The storage of large quantities of methane as hydrates on the continental shelf has also raised questions regarding the importance of hydrates in the global carbon cycle, and the potential role of hydrate formation and dissociation (in response to changing ocean conditions) in past and future climate change [6–9].

The majority of hydrate deposits discovered to date are of biogenic origin, meaning the gas in the hydrates was produced through microbial transformation of organic carbon. These processes produce mainly methane, leading to sI methane hydrate being the most prevalent hydrate type in nature [8]. However, hydrates formed from mixed biogenic–thermogenic gases [10,11] and pure thermogenic [12] gases have also been found in areas such as the Gulf of Mexico [12], the Caspian Sea [13], and Barkley Canyon [14]. Thermogenic gases are produced by the thermal cracking of kerogens at temperatures greater than 373 K. This process creates a significant amount of hydrocarbons heavier than methane, leading to sII and even sH hydrates [15], with C_{2+} contents in excess of 20–30% [8,16].

Along with the ability of hydrates to concentrate gas, certain gas components have preferential occupancy in the hydrate phase. For example, in constant volume laboratory experiments with a methane + propane mixture, propane was shown to be denuded from the vapor phase during hydrate formation [17]. Initial formation of a mixed sII methane + propane hydrate was followed by formation of sI methane hydrate after the propane was exhausted. The order in which the gases are consumed reflects the relative thermodynamic stability of the resulting hydrate phase. Thus the increased number of components in thermogenic gas mixtures can lead to variations in hydrate composition and structure as formation initially strips the preferential hydrate forming compounds from the vapor phase. Intrinsic hydrate properties, such as thermal conductivity and *P*, *T* conditions for dissociation, are strongly dependent on composition and structure. A good understanding of hydrate formation processes is therefore necessary to accurately model hydrate stability, with implications for either the recovery of gas from hydrate deposits as a fuel source, and/or the prediction of continental shelf stability. It should also be noted that the stability of hydrates is controlled by the equality of chemical potential in the solid, aqueous, and free gas states and thus hydrates will also respond to changes in aqueous boundary composition as the fluids bathing them evolve.

Thermogenic hydrate systems are most often considered to be supplied from deep petroleum reservoirs [8]. Modeling efforts to understand the sequence by which these thermogenic hydrates form have been undertaken [18]. In these models, gas from a deep reservoir migrates upwards through the sediment column. During this migration, hydrate formation sequences cause the composition of the rising gas to change due to chemical fractionation.

While this model was successfully fit to calculate observed properties such as vent gas composition at a hydrate site in the Gulf of Mexico, the hydrate formation mechanism in this model is by no means proven. For example, deep ocean experiments in which gas was bubbled through bulk seawater showed near instantaneous formation of a hydrate skin around the bubbles upon injection [19]. When gas was bubbled in clay sediments saturated with seawater, channels opened allowing the gas to flow. These channels became coated with white hydrate [19]. In both of these cases, the hydrate could act as a barrier to further mass transfer, resulting in non-uniform gas composition changes with depth. This type of phenomenon presents a challenge in terms of modeling.

In situ Raman spectroscopy is a tool that can be used to help understand the formation and growth of multi-component hydrates in the ocean. Raman spectroscopy determines molecular level information about hydrates. Because Raman is a local technique, meaning that only a small volume is sampled, spatial variation in the composition and structure of the hydrate can be assessed by scanning the laser across the surface of the bulk sample. Initial field work to qualify the *in situ* Raman technique on hydrates yielded results comparable with those in controlled laboratory settings [20]. The first field expedition using Raman spectroscopy to measure naturally occurring ocean hydrates on the seafloor was performed at Hydrate Ridge in 800 m water depth [21]. The hydrate formed was associated with cold gas venting seeps. *In situ* measurements showed mainly sI methane hydrate in a bubble fabric; along with small quantities of hydrogen sulfide heterogeneously distributed in the hydrate. Measuring gas composition in bulk hydrate samples gives an overall picture of the hydrates present. With the addition of techniques such as Raman spectroscopy, direct evidence for the presence and spatial heterogeneity of different hydrate structures/compositions can be determined. This information is essential for understanding and correctly modeling hydrate formation, growth, and dissociation mechanisms. For example, hydrate will have a different response to changes in *P*, *T* conditions if it has a homogenous composition versus if small ingrowths of less stable hydrate exist in a bulk sample.

Here we report on new oceanic field experiments performed using the *in situ* Raman technique along with visual observations from a remotely operated vehicle (ROV) to investigate multi-component hydrate phase behavior. For a field experiment following an equivalent protocol to the binary methane + propane laboratory experiments [17], a synthetic complex natural gas mixture, with an eight component com-

Table 1
Molar composition of the feed gases and hydrate

Component	Molar feed composition		Molar hydrate composition		CSMGem (averaged)
	Synthetic gas mixture	CSMGem mixture	Barkley Canyon	CSMGem (initial)	
Methane	92.5	93.0	75.4	70.2	82.3
Ethane	3.8	4.0	11.4	5.1	10.4
Propane	1.9	2.0	5.7	18.6	5.5
i-Butane	0.4	0.4	1.2	5.6	0.8
n-Butane	0.4	0.4	2.2	0.5	1.1
Neo-pentane	0.1				
i-Pentane	0.1	0.1	0.7		
n-Pentane	0.1	0.1	0.3		
Air	0.4				
C_{6+}			3.1		

The feed gas compositions are given for the synthetic natural gas mixture and the mixture used in CSMGem condensation calculations. Barkley Canyon hydrate composition from [15], the initial CSMGem hydrate composition and the average CSMGem hydrate composition over 22 condensation steps.

position chosen to simulate a thermogenic natural gas, was used to form hydrates at constant P, T. In addition, preliminary results are reported from an expedition to Barkley Canyon, a known site of thermogenic gas hydrates [14]. The observed compositions of the synthetic and natural thermogenic hydrates are compared to thermodynamic model predictions allowing a possible hydrate formation mechanism to be inferred.

2. Experimental methods

2.1. Gas mixture and hydrate cell

A synthetic natural gas mixture (92.5% CH_4, 3.8% C_2H_6, 1.9% C_3H_8, 0.4% *i*-C_4H_{10}, 0.4% *n*-C_4H_{10}, 0.1% *i*-C_5H_{12}, 0.1% *n*-C_5H_{12}, and 0.1% neo-C_5H_{12}) was chosen to simulate a typical thermogenic natural gas based on a published analysis of vent gases from regions of hydrate formation ([14], see Table 1). The gas was mixed by Scott specialty gas and the composition was verified in the MBARI laboratories using gas chromatography. Table 2 gives both the simple hydrate structure formed and the hydrate cages the molecules in the gas mixture can occupy.

The synthetic natural gas hydrate was formed on the seafloor in the Monterey Canyon in the Monterey Bay at a water depth of 1023 m (T = 277.0 K, P = 10.44 MPa, salinity = 34.5 psu). Conditions were measured both on deployment and recovery, but not during the given formation time. While monitoring of the pressure and temperature was not performed during the experiment, both the deployment and recovery indicated long term stability at this site. Between both visits, temperature varied by less than 0.1° and salinity varied by only 0.01. In addition, measured conditions were similar to previous expeditions in the experiment area (276.65 K [22] and 277.0 K [20]). The method of hydrate formation is described elsewhere [20], and briefly summarized here. The hydrate was formed in a 3.2 liter (264 mm × 124 mm) cylindrical Pyrex cell. The cell was sealed by two end caps with gas and water lines run into the cell to allow both ambient seawater and the synthetic gas mixture to be pumped into the cell at depth. At the seafloor, the cell was flushed with ambient seawater before injecting the synthetic natural gas mixture into the bottom of the cell in 1–5 s bursts through a hydraulically actuated valve. After allowing 65 days for formation, the hydrate cell was revisited and interrogated using both visual observation and Raman spectroscopy.

Table 2
Simple hydrate formed and cages occupied by the molecules in the natural gas mixture

	Simple hydrate formed	Occupied cages
Methane	sI	5^{12}, $5^{12}6^2$, $5^{12}6^4$, $4^35^66^3$
Ethane	sI	$5^{12}6^2$, $5^{12}6^4$
Propane	sII	$5^{12}6^4$
i-Butane	sII	$5^{12}6^4$
n-Butane	sII[a]	$5^{12}6^4$
Neo-pentane	sII[a]	$5^{12}6^4$
i-Pentane	sH[a]	$5^{12}6^8$
n-Pentane	sH[b]	$5^{12}6^8$

[a] Requires help-gas molecule, e.g. CH_4.
[b] Requires help-gas molecule + sH co-guest.

2.2. Seagoing Raman spectrometer—DORISS II

Deep ocean Raman *in situ* spectrometer (DORISS) II is a second-generation modified seagoing Kaiser Optical Systems Inc., Raman spectrometer. This spectrometer, first deployed in 2005 [23], is a lighter, more compact and robust version of the original DORISS system [24–26]. For the Barkley Canyon expedition, the original fiber optic cables were also replaced with much improved pressure compensated fiber optic cables that eliminated signal losses that occurred in the earlier design. The spectrometer consists of a 532 nm Nd:YAG laser, a holographically filtered probe head, a holographic duplex grating, and a 512 × 2048 front illuminated CCD camera from Andor Technology. The spectral range of DORISS II is 100–4400 cm^{-1}. The duplex grating splits the spectrum into two strips on the face of the CCD chip providing a mapping of ~1 cm^{-1} per pixel. The spectrometer and on-board computer for communications and control were packaged in a titanium housing rated to 4000 m depth. Power and ethernet communications to the instrument were provided through the ROV tether.

The optical probe head with a stand-off sampling optic (f/3) was contained in a titanium housing with a glass dome win-

dow. A sampling geometry with 180° backscattering was used. A focusing mechanism, consisting of a motor driven stage inside of the housing, moved the probe head within the housing providing a working distance of 152 mm in water. The sampling volume can be estimated from the depth of field and the laser spot size. The depth of field was 3 mm in water, as determined experimentally using a polished silicon wafer. The diameter of the laser spot size was on the order of tens of microns.

Frequency and intensity calibrations were performed in the laboratory and on the ship prior to deployment, using neon emission and white light. The laser power output from the probe head was measured on deck to be around 34 mW. During deployment, a thin diamond wafer placed in the beam path inside the probe head served as a frequency calibration reference; the 1332 cm^{-1} diamond Raman line was superimposed on all collected spectra. Spectra were acquired using KOSI's HoloGRAMS software, where dark spectrum subtraction and wavelength and intensity correction were performed by HoloGRAMS during acquisition and the processed spectra were saved in generic spectrum (spc) format. Typical accumulation times for the hydrate samples varied between 5 and 20 s for individual collection and cumulatively summed over 5–20 collections.

A stand-alone precision underwater positioner (PUP) was employed along with the Raman probe to provide the ability to analyze solid, opaque samples subsea [27]. The DORISS II Raman probe head was mounted on this stand-alone positioner to provide precise positioning of the DORISS II probe head in a horizontal orientation. Once at the seafloor, PUP is offloaded from the ROV onto the seafloor. This decoupled the optical beam from the intrinsic vibrations of the ROV. Controlled by a shipboard scientist, PUP is capable of moving the probe head with a precision of 0.1 mm in three dimensions—two linear and one rotational. The focus stage inside the probe head provided an additional dimension of movement.

3. Results and discussion

3.1. Synthetic gas experiment—visual observations of the hydrate phase

To stimulate hydrate formation, the initial injection of gas bubbles was into the bottom of the cell. This approach was taken for two reasons: (1) to enhance mass transfer for saturation of the aqueous phase with the synthetic gas mixture, and (2) to maximize hydrate formation. Beyond the two practical reasons given for the experimental approach, the method of injecting gas bubbles at the bottom of the cell also simulated a possible natural hydrate formation mechanism. Rising bubbles contribute to natural hydrate formation in areas such as cold vent sites [28,29]. It should be noted, however, that unlike natural systems, there were no sediments in this work. At the seafloor conditions (T = 277.0 K, P = 10.44 MPa, salinity = 34.5 psu), the thermal driving force to form hydrate was greater than 14 K. By bottom filling, each burst of buoyant gas injected into the cell forced the gas bubbles to travel up through the seawater phase; as opposed to injection from the top, wherein all subsequent injections would have been into the vapor phase with a single contact interface between the two phases. Visual observations of the gas injection show that a hydrate skin formed on the gas bubbles almost immediately on contact with seawater. This observation agrees well with earlier ocean field work using methane and a mixed gas containing methane, ethane, and propane [19,30]. The cell was shaken intermittently during filling causing white particles, assumed to be hydrate-encrusted gas bubbles, to move freely in the aqueous phase. It could not be determined if gas bubbles without hydrate skins or fully converted hydrate particles were also present. After mixing, the buoyant particles resettled with more efficient packing; becoming more consolidated at the top of the cell. This process of gas injection and cell agitation was repeated multiple times. It was observed that the freshly formed hydrate particles were quickly dispersed in the aqueous phase during shaking; although the more consolidated hydrate particles showed stronger adhesion and temporarily resisted dispersion.

The ocean setting provided stable pressure and temperature conditions (see Section 2.1); however, the setting also limited the frequency of observation of the cell. Therefore, we were only able to observe the initial hydrate formation and the hydrate that had formed by the return visit 65 days later. The top of the cell was observed to be filled with an annealed hydrate mass (Fig. 1). The adhesion forces appeared to have become much more significant over time and the hydrate did not move when the cell was shaken. The conversion of the gas phase and annealing of the hydrate agreed with previous work using a methane + ethane mixture [20]. Close inspection of the cell showed that there was a small layer of free gas present at the top and bottom of the hydrate, with a hydrate skin visible at the interface between the free gas and the bulk seawater in the bottom of the cell.

3.2. Synthetic gas experiment—in situ Raman measurement of the hydrate phase

The visual observations showed that hydrate formed rapidly around the injected gas bubbles, and after time converted to an annealed hydrate mass; however, visual observation could not provide indications of the homogeneity (or otherwise) of the multi-component hydrate's structure or composition. To determine this information, a vertical profile of Raman hydrate spectra (200–4000 cm^{-1}) was collected along the vertical axis of the reaction cell using PUP to scan the laser down the hydrate mass.

Methane was the main constituent in the gas mixture and, of the gas components in the hydrate phase, provided the strongest Raman peaks. In Fig. 1, the C–H stretching region of the vertical Raman profile is shown along with the approximate section of the hydrate sample where each spectra was recorded. The C–H stretching region contains the methane hydrate peaks at 2904 (sI or sII large cages) and 2914 (sI or sII small cages) cm^{-1} [31]. From the methane peaks, two compositional regions could be observed. Near the top and the bottom of the hydrate mass, the intensity of the 2904 cm^{-1} peak was much less than the 2914 cm^{-1} peak. In the middle of the cell, the intensities of the 2904 and 2914 cm^{-1} were similar.

While the methane peaks can be used to determine if methane is in the large or small hydrate cages, additional structural iden-

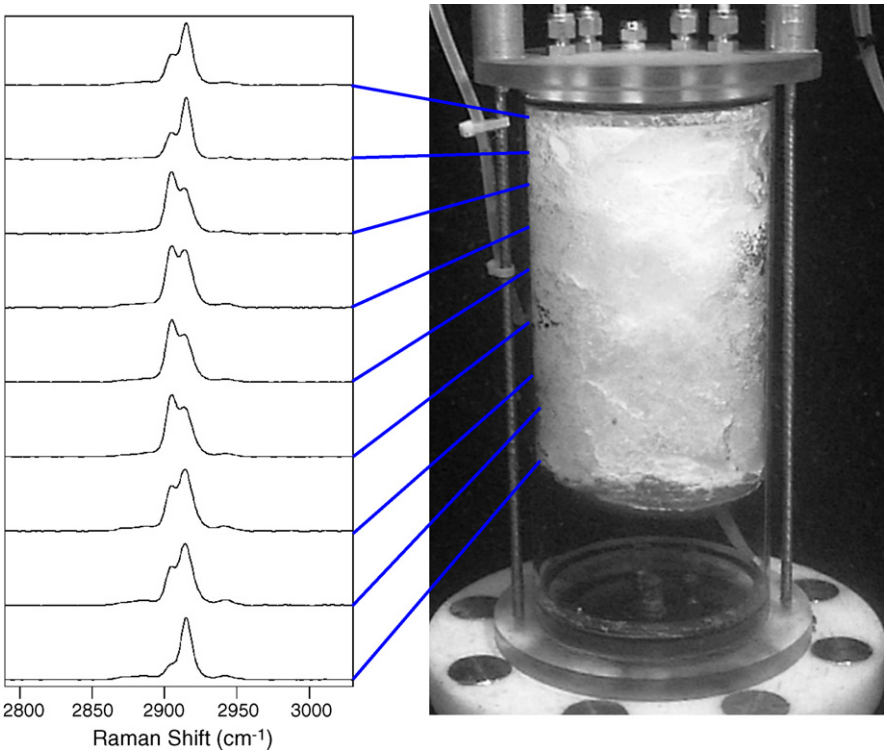

Fig. 1. Vertical Raman profile of the synthetic natural gas hydrate formed in the Monterey Bay. The approximate section of the hydrate were each spectra was taken is indicated.

tification is more ambiguous as the Raman shift for methane in each cage type is indistinguishable between sI and sII hydrates for the spectral resolution used in this study. However, the ratio of the large and small cage peaks can aid structural identification when considered in conjunction with the presence/absence of Raman peaks from other gas components in the C–C stretching region of the spectra. In order to evaluate whether sI or sII is present from the methane peak areas, an argument must be made about the cage distributions between the structures [32]. For methane-rich mixtures with hydrate guests which do not fit in the small cages, the intensity ratio of methane in the sII large and small cages should be less than 0.5. This is because, in such mixtures, methane will occupy most of the small cages of sII and the larger guest will occupy at least some of the sII large cages, along with methane. For the case of the same mixture forming sI, the methane will again occupy most of small cages. The large guest and methane will compete for the large cages. Therefore, depending on the system, the methane occupancy ratio could vary between 0 and around 3. Combining this information allows better understanding of the two compositional regions.

A representative spectrum from the top/bottom region is shown in Fig. 2. The ν_3 C–C stretch of ethane in the large cage of sII hydrate (sII $5^{12}6^4$) can be clearly seen at 992 cm^{-1} (Fig. 2a), while the corresponding peak for ethane in the large cage of sI hydrate (sI $5^{12}6^2$, 1001 cm^{-1}) is absent, strongly suggesting the presence of a sII dominated hydrate [33]. This assignment of sII is in agreement with the ratio of the methane peaks (2904:2914 cm^{-1}) being around 0.1 (Fig. 2b).

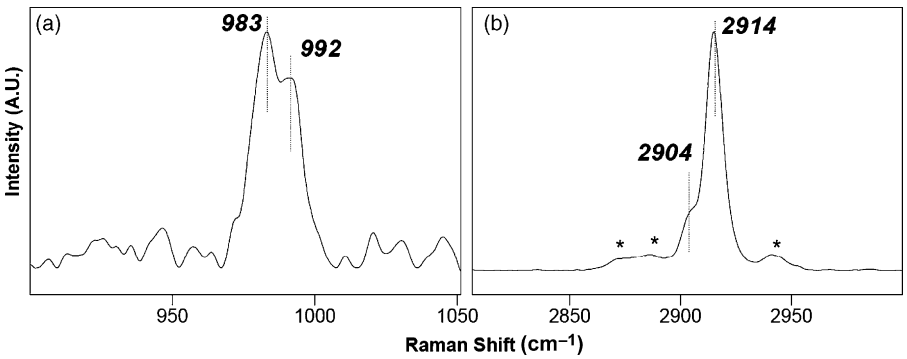

Fig. 2. Representative Raman spectrum from the top/bottom area of the cell of synthetic natural gas hydrate formed in the Monterey Bay (10.44 MPa, 278 K, collection time: 150 s). Panel (a) shows the C–C stretching region. Panel (b) shows the C–H stretching region. Peaks labeled at 983 cm^{-1} (SO_4^{2-}, dissolved), 992 cm^{-1} (C_2H_6 $\nu 3$, sII $5^{12}6^4$), 2904 cm^{-1} (CH_4 $\nu 1$, sII $5^{12}6^4$), 2914 cm^{-1} (CH_4 $\nu 1$, 5^{12}). Asterisks marked for the C–H stretching modes of C_{2+} molecules in the hydrate phase.

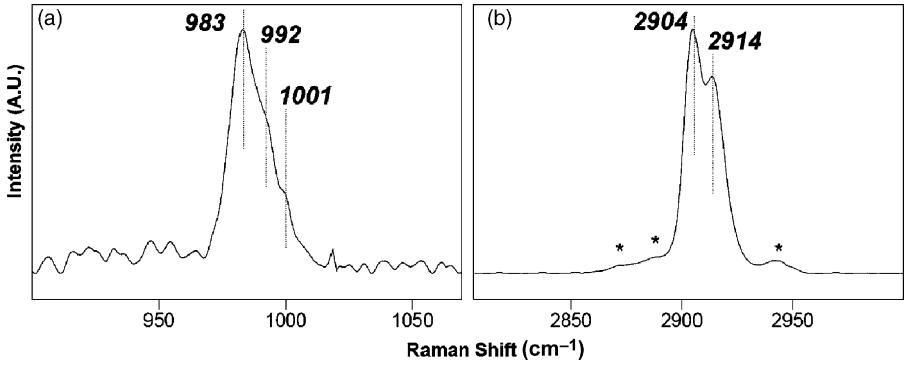

Fig. 3. Representative Raman spectrum from the middle area of the cell of synthetic natural gas hydrate formed in the Monterey Bay (10.4 MPa, 278 K, collection time: 150 s). Panel (a) shows the C–C stretching region. Panel (b) shows the C–H stretching region. Peaks labeled at 983 cm^{-1} (SO_4^{2-}, dissolved), 992 cm^{-1} (C_2H_6 $\nu1$, sII $5^{12}6^4$), 1001 cm^{-1} (C_2H_6 $\nu3$, sI $5^{12}6^2$), 2904 cm^{-1} (CH_4 $\nu1$, sI–sII large cage), 2914 cm^{-1} (CH_4 $\nu1$, sI–sII small cage). Asterisks marked for the C–H stretching modes of C_{2+} molecules in the hydrate phase.

A representative spectrum from the middle region is shown in Fig. 3. In this case, the ν_3 C–C stretch of ethane was observed at both 992 (C_2H_6, sII $5^{12}6^4$) and 1001 (C_2H_6, sI $5^{12}6^2$) cm^{-1}, shown in Fig. 3a. This result indicated that a mixture of sI and sII was present [33]. Applying the same argument as outlined above, the presence of both sI and sII is consistent with the relatively close intensity ratio observed for the methane peaks in this region (Fig. 3b), where the 2904:2914 cm^{-1} peak ratio varied from 0.53 to 1.0 (Fig. 1). Because Raman is a point measurement, the variation present in the ratio of the methane peaks reflects the compositional heterogeneity in the sample.

3.3. Synthetic gas experiment—recovery and laboratory hydrate measurements

After the *in situ* Raman measurements were completed the cell was recovered to the ship deck by the ROV. The cell was open to the ambient ocean conditions during recovery through narrow bore tubing to allow pressure accommodation. The pressure decreased and temperature increased continually as the ROV ascended through the water column, over a period of around 30 min.

As the ROV ascended, the hydrate became unstable and bubbling was observed. Similar to laboratory experiments on hydrate plug dissociation [34] where heat transfer controls the dissociation, radial dissociation was initially dominant over axial dissociation due to the greater surface area with the surroundings. This resulted in a gas-filled gap between the hydrate and the cell walls (Fig. 4a and b). After the gas-filled gap formed, radial dissociation slowed due to the low thermal diffusivity of the gas phase. Axial dissociation became dominant with vigorous bubbling observed at the hydrate/water interface in the cell, as seen in Fig. 4c, and a marked decrease in the length of the hydrate mass.

On deck, the hydrate was removed from the cell, quenched in liquid nitrogen, and sent to the Center for Hydrate Research (CHR) laboratory in a liquid nitrogen dry shipper. Fig. 4d shows the hydrate on deck after recovery; the recovered solid was very friable.

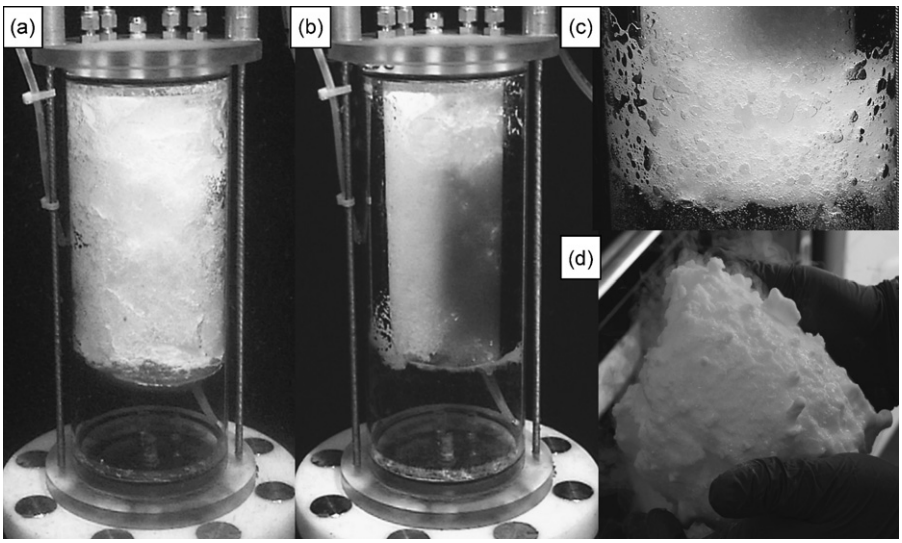

Fig. 4. Synthetic natural gas hydrate formed in the Monterey Bay during non-pressurized recovery. Panel (a) shows the hydrate on the seafloor. Panels (b and c) show the hydrate during non-pressurized recovery: in (b) visible gas observed between the hydrate and the cell wall, indicated radial dissociation and in (c) vigorous dissociation observed for the hydrate at the hydrate/water interface. Panel (d) shows the hydrate on deck after non-pressurized recovery.

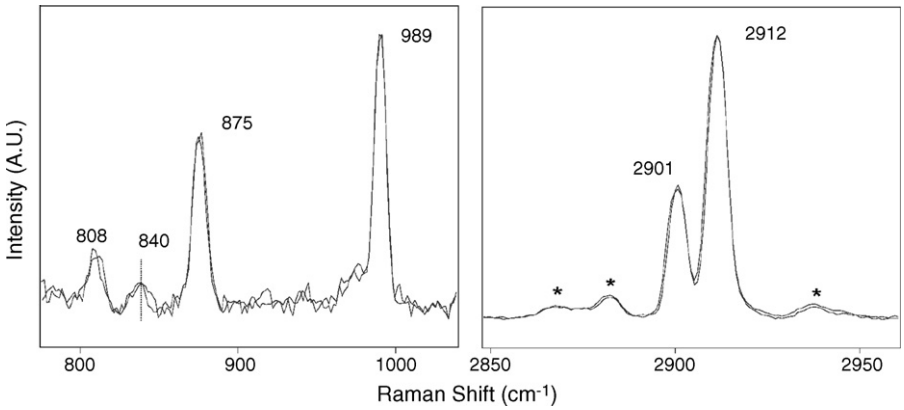

Fig. 5. Synthetic natural gas hydrate recovered and measured in the laboratory using Raman spectroscopy at 77 K. Peaks labeled at 808 cm^{-1} (i-C_4H_{10} ν7, sII $5^{12}6^4$), 840 cm^{-1} (n-C_4H_{10}, sII $5^{12}6^4$), 875 cm^{-1} (C_3H_8 ν8, sII $5^{12}6^4$), 989 cm^{-1} (C_3H_8 ν3, sII $5^{12}6^4$), 2901 cm^{-1} (CH_4 ν1, sII $5^{12}6^4$), 2912 cm^{-1} (CH_4 ν1, sII 5^{12}). Asterisks marked for the C–H stretching modes of C_{2+} molecules in the hydrate phase.

Raman spectroscopy was used to analyze the recovered hydrate samples in the laboratory. Because the remaining hydrate fractured into many pieces, three random spots were selected for measurement. The recovery of the sample in rapidly changing P, T conditions caused dissociation of both the sI and sII phases. Qualitatively using the relative intensity of the water to hydrate guest Raman peaks, a significant fraction of the sample was measured to be water ice. Although there were no temperature measurements of the hydrate phase during recovery, formation of ice during rapid dissociation of hydrate has been routinely observed in the laboratory [34], and was most likely the cause of ice formation in this case.

While both hydrate phases experienced dissociation, some sII hydrate remained. Fig. 5 shows an overlay of the C–C and C–H stretching regions from the three laboratory Raman spectra of the recovered hydrate. The surprisingly close comparison between these spectra indicates a homogenous composition. The predicted stability of the incipient hydrate formed (the first hydrate phase to nucleate) from the synthetic gas mixture at 277 K was calculated with CSMGem [35] using a comparable gas composition given in Table 1 (CSMGem mixture), and compared to the stability of pure methane hydrate. The incipient hydrate formed from the synthetic gas mixture is stable at 1.3 MPa; while methane hydrate needs 3.9 MPa. This difference in stability combined with the lower overall phase fraction of sI correlated with the presence of only sII in the recovered sample.

3.4. Preliminary measurements of natural thermogenic hydrate at Barkley Canyon

The seafloor hydrates at Barkley Canyon were originally "discovered" by a fishing trawler [36]. Subsequent studies of the area revealed exposed thermogenic hydrates stained yellow with a petroleum condensate [14,37]. A deep petroleum reservoir is thought to be supplying this hydrate accumulation [14]. Laboratory analysis on recovered samples has shown that sII hydrate along with small quantities of sH exist at this site [15].

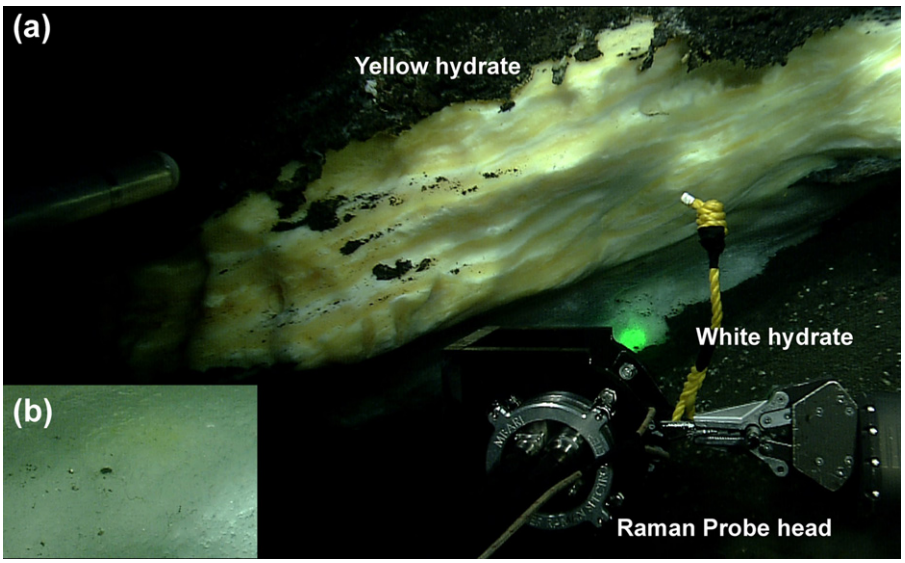

Fig. 6. The "double mound" site at the Barkley Canyon. Panel (a) shows an exposed hydrate face with both the yellow and white hydrate fabric, along with Raman probe head positioned for *in situ* sampling. Panel (b) shows a close up of the white hydrate fabric.

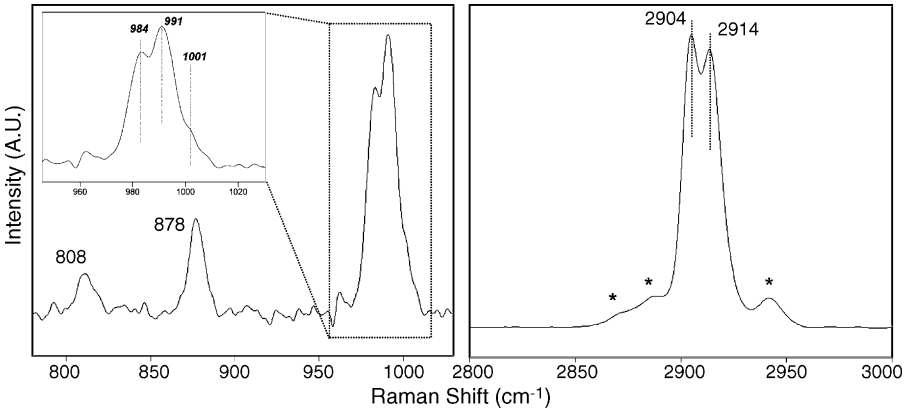

Fig. 7. Representative Raman spectrum from natural hydrate at Barkley Canyon (8.5 MPa, 278 K, collection time: 150 s). Peaks labeled at 808 cm^{-1} (*i*-C_4H_{10} ν7, sII $5^{12}6^4$), 878 cm^{-1} (C_3H_8 ν8, sII $5^{12}6^4$), 984 cm^{-1} (SO_4^{2-}, dissolved), 991 cm^{-1} (C_2H_6 ν1, sII $5^{12}6^4$), 1001 cm^{-1} (C_2H_6 ν3, sI $5^{12}6^2$), 2904 cm^{-1} (CH_4 ν1, sI–sII large cage), 2914 cm^{-1} (CH_4 ν1, sI–sII small cage). Asterisks marked for the C–H stretching modes of C_{2+} molecules in the hydrate phase.

In August 2006, an MBARI expedition studied these hydrate outcrops further [32]. An exposed face of one of the hydrate mounds, named "double mound" by the earlier Canadian expeditionary team, is shown in Fig. 6. While most of the hydrate was stained to various degrees with the yellow condensate, a layer of white hydrate underlying the yellow-stained hydrate was also observed. *In* situ Raman measurements were performed on both the "yellow" hydrate and the "white" hydrate. Raman spectra of the yellow hydrate had a high degree of background interference, caused by fluorescence of the condensate, reducing the amount of information obtained in the Raman measurement. However, the white hydrate was fluorescence-free and Raman shifts for various hydrate components could be identified. Both the color of the white hydrate and lack of fluorescence indicated that the condensate phase was not associated with this hydrate.

Different locations on the white hydrate were sampled. Along with vibrations for methane, Raman shifts for ethane, propane, and butane in the sII lattice were also present. In the C–H stretching region, Fig. 7 shows that the relative intensity for methane in the large and small cages is similar. This result agrees with the middle region from the synthetic experiment (Section 3.2) where it was determined that a mixture of sI–sII was present. Focusing on the Raman shift for ethane in the natural hydrate (Fig. 7, insert), a peak at 991 cm^{-1} is accompanied with a shoulder at 1001 cm^{-1}, confirming the coexistence of sI and sII.

Coexistence of sI and sII in nature has been directly measured for only one other site, Lake Baikal in Russia [11]. This was attributed to chemical fractionation from hydrate formation or possible metastable phases, observed in laboratory work when gas concentrations were close to where a structural transition occurs [38,39].

4. Comparison of observations to modeling and implications for hydrate formation mechanisms

4.1. Co-existence of sI–sII—thermodynamic predictions for the synthetic hydrate system

In situ Raman measurements of hydrate formed from a synthetic natural gas mixture detected two distinct composition regions: a sII dominated region, and a mixed sI–sII region. Here we examine potential hydrate formation mechanisms that could result in this phase distribution. One likely explanation is that sII-forming hydrocarbons were denuded from the gas mixture during hydrate formation. Because the hydrate was formed in a closed system, the sII-forming hydrocarbons become concentrated in the initial hydrate formed causing the gas mixture to become enriched in methane. Similar to previous laboratory work [17], the formation of sII continued until the concentration of the sII-forming molecules was so depleted that sI hydrate became the stable structure at the gas–liquid boundary layer.

In order to investigate the effect of chemical fractionation on the resultant hydrate composition in a more quantitative manner, CSMGem [35] was used to model changes in the composition of both the gas and hydrate phases during hydrate formation. For these calculations, an initial molar feed mixture was used with 93% CH_4, 4% C_2H_6, 2% C_3H_8, 0.4% *n*-C_4H_{10}, 0.4% *i*-C_4H_{10}, 0.1% *n*-C_5H_{12}, and 0.1% *i*-C_5H_{12}. This mixture composition is given in Table 1 (CSMGem mixture) and is a close representation of the experimental gas composition used. Because CSMGem performs constant volume flash calculations, a series of discrete condensation steps were carried out to model the evolution of the gas and hydrate phase compositions during the hydrate growth process. Each condensation step was based on the conversion of 1 mol of liquid water to hydrate, in contact with 100 mol reservoir of gas. Based on conditions at the seafloor during the controlled field experiment (see Section 2.1), the flash was calculated at a pressure of 10.44 MPa and a temperature of 276.75 K.

As shown in Fig. 8, *i*-butane and propane are denuded from the gas phase first. Ethane is also denuded until sI became the stable structure. The other heavy components (*n*-C_4H_{10}, *n*-C_5H_{12}, and *i*-C_5H_{12}) are predicted to have little to no filling in the sI or sII hydrate phases. As ethane, propane, and i-butane are concentrated in the hydrate phase, there is a slight increase in the mole fractions of *n*-C_4H_{10}, *n*-C_5H_{12}, and *i*-C_5H_{12} in the vapor phase; however, this slight increase is insufficient to cause sII (*n*-C_4H_{10}) or sH (*i*-C_5H_{12}) formation and these components are excluded from the hydrate, consistent with the results of Sassen et al. [40].

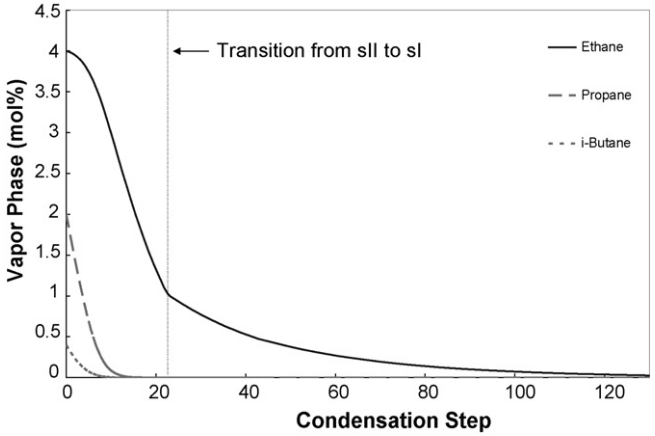

Fig. 8. Changes in the vapor phase composition during hydrate formation predicted using CSMGem. A constant volume flash at 10.44 MPa and 276.75 K was performed with a gas reservoir of 100 mol and 10 mol of water in each condensation step.

The results of this thermodynamic modeling suggest that the growth of hydrate from a single gas/water interface would result in a steady gradient in the concentration of sII-forming hydrocarbons in the hydrate mass. Following the complete denuding of propane and *i*-butane, formation of sII would continue until the ethane concentration was sufficiently depleted for sI to become the favorable phase formed; this results in a distinct transition from a sII hydrate to a sI hydrate (Fig. 8). However, the observed spatial variation in composition in our synthetic hydrate experiment was markedly different, with existence of sII in the top and bottom regions of the sample, while both sI and sII existed in the middle region of the sample. Our visual observations of the initial formation show that hydrate mass did not grow from the bulk gas/water interface. As the gas mixture was added to the cell, a hydrate skin appeared to form around the bubbles. This skin could have acted as a mass transfer barrier effectively making each bubble an individual hydrate reactor.

As the gas mixture was converted to sII hydrate, the gas contained in each reactor became denuded in sII-forming compounds until the gas composition was primarily methane. The system then began to form sI hydrate. The coexistence of sI and sII in the middle of the cell was consistent with this hypothesis.

In the sample top and bottom, however, mainly sII was measured. The structural difference in the sample ends from the middle region might be explained by contact with a free gas phase. This free gas phase would be less affected by denuding than the individual hydrate-coated bubbles, for the same amount of hydrate formation, due to the larger relative mass of gas available. However, the question remains as to why this free gas phase had not converted to hydrate. Thermodynamically, this system was approaching equilibrium but driving forces were not entirely absent. In achieving equilibrium, the remaining vapor phase must be consumed unless an increase in salinity precludes further hydrate formation.

Hydrate formation excludes salt leading to increased salinity in the remaining free water. When on the seafloor, the hydrate cell was effectively closed with minimal communication to the ambient seawater. Raman analysis provided an estimate of the salinity inside of the cell through a comparison of the seawater spectra collected inside and outside of the cell were collected (Fig. 9, spectral processing described in [23]). Laboratory work has demonstrated that the area of the sulfate Raman peak varies linearly with salinity [41]. The increased intensity of the sulfate peak inside the cell with respect to ambient bottom seawater is quite pronounced (Fig. 9a). As the seawater salinity is known (34.5 psu), and the sulfate peak area is zero in fresh water, a linear fit can be assumed to estimate a modified salinity inside the hydrate cell of 39 ± 1 psu. Differences between the two spectra are also apparent in the O–H stretching region (Fig. 9b and c). Firstly, a small peak for dissolved methane inside the cell was detected at around 2910 cm^{-1} (Fig. 9c) Secondly, a small but resolvable shift is observed in the peak intensity distribution across the O–H stretching region. Fig. 9c shows a close up of the O–H stretching peaks. In the low wavenumber region (~3250 cm^{-1}), the intensity of the ambient seawater spectrum is greater than that of the modified seawater inside the cell, where as in the high wavenumber region (~3425 cm^{-1}) the relative intensities are reversed. This is consistent with previous observations of the effect of increased salinity on the water O–H stretching region and can be interpreted as reflecting decreased hydrogen bonding between the water molecules (via disruption through formation of solvation spheres) [42]. At 10.44 MPa, the measured increase in salinity will only decrease the hydrate formation temperature for methane hydrate from 284.9 to 284.7 K. Because pure methane hydrate is the least stable hydrate (compared to when heavy hydrocarbons are also present) and the seafloor temper-

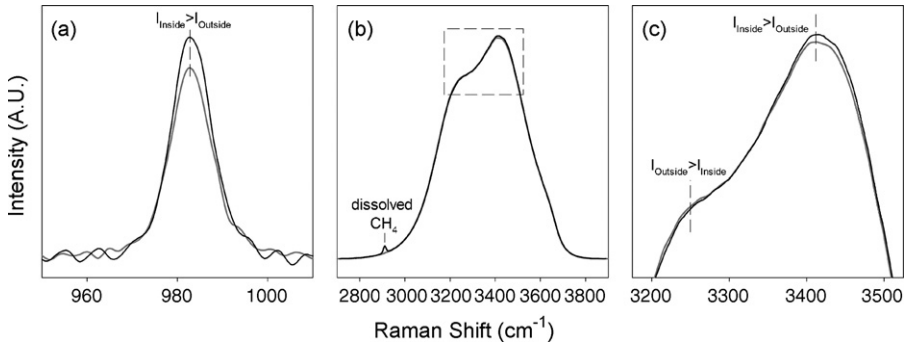

Fig. 9. Raman spectra of seawater at the seafloor both inside (black line) and outside (grey line) of the hydrate cell. (a) Sulfate peak; (b) water peak; (c) expanded view of water peak.

ature was 277.0 K, salinity was not inhibiting further hydrate formation.

Because the thermodynamic conditions were sufficient for hydrate formation, a transport limitation provides an explanation for this lack of complete consumption of the free gas phase. In the cell, the hydrate mass was separated from the bulk water by a layer of free gas. A hydrate skin was observed at the interface of the free gas and bulk water phases, limiting further conversion to hydrate. The gas layer at the top of the cell was even more removed from free water for further hydrate formation.

4.2. Co-existence of sI–sII—possible growth mechanism in the natural system

Similar to the synthetic multi-component hydrate, the white hydrate measured at Barkley Canyon showed a coexistence of sI–sII phases in close contact [32]. In both cases, sI and sII hydrate were distributed heterogeneously through the bulk hydrate. Denuding of the gas phase is a very plausible explanation for the synthetic gas experiment and, hence, could apply to the natural hydrate system. In addition, rising bubbles have been shown to model hydrate formation in natural gas venting systems [28].

This conjecture is supported by further consideration of the thermodynamic modeling. The predicted hydrate composition for the first condensation step and the average hydrate composition after 22 condensation steps (up to the point where sI became the stable structure) are shown in Table 1 (CSMGem (initial) and CSMGem (averaged), respectively). The predictions show that the hydrate initially forms with higher concentrations of heavy sII-forming molecules (C_{3+}) and lower concentrations of ethane than those reported from recovered natural samples. However, the average hydrate composition, using the gas-limited mechanism, shows a result very comparable to those reported for natural hydrate at Barkley Canyon [14].

While the above calculation does not prove the formation mechanism of this white hydrate at the Barkley Canyon, the results of the controlled field experiment combined with the thermodynamic modeling show that denuding of the gas phase is a viable growth pathway when studying natural hydrate formation from multi-component gas streams.

4.3. Initial suggestions on formation of sH in complex hydrate systems

The presence of sH in natural hydrates has been inferred [43] and recently directly measured from Barkley Canyon hydrates [15,32], where the yellow hydrate fabric at Barkley Canyon consisted sII with a small amount of sH present. Denuding of a complex multi-component gas mixture during hydrate formation could also lead to this result.

As stated in Section 4.1, the concentration of *i*-pentane in the CSMGem feed mixture was not sufficient to result in sH formation during hydrate growth. In order to investigate this further, a binary methane + *i*-pentane system was flashed at 10.44 MPa and 276.75 K to determine the minimum concentration of *i*-pentane required to form sH. At these *P*, *T* conditions, a surprisingly high concentration of over 49 mol% *i*-pentane is required. However, at the same temperature but at a lower pressure, e.g. 5 MPa, only 1.1 mol% is needed; this indicates the important role pressure can play in determining hydrate structure within these systems.

In addition to the considerable influence pressure can have, the effect of the sH-forming guest molecule was also investigated. Using the same feed gas mixture (CSMGem mixture) but methylcyclohexane substituted for *i*-pentane, a series of condensation steps were performed. In this case, following the denuding of the heavy sII-formers, such as i-butane and propane, a sII–sH coexistence was predicted to occur.

Furthermore, it is plausible that a sI–sII–sH coexistence could occur. If a natural gas containing sH-forming molecules is used to form hydrate, the stable hydrate structure would initially be sII. When the sII molecules are consumed, methane would combine with the sH-formers resulting in sH. When the concentration of sH-formers is lowered, the remaining methane could then form sI hydrate. This has not yet been observed in nature.

From this analysis using CSMGem, sH formation occurs only when the concentration of sII-forming molecules is exhausted and a sufficient concentration of sH-forming molecules is available. However, the required concentration is a function of both the specific sH-forming molecule and the *P*, *T* conditions.

5. Conclusions

Based on our *in situ* Raman measurements and observations of synthetic hydrate formation from a complex feed gas in combination with thermodynamic modeling, a hydrate growth mechanism was proposed that likely also contributes to natural hydrate formation processes. In the synthetic experiment, hydrate growth occurred both from gas bubbles separated from the bulk vapor phase by hydrate membranes, resulting in an inter-mixed sI–sII phase, and in regions in contact with the bulk vapor phase, in which only sII hydrate was detected. The spatial heterogeneity of the mixed sI–sII region was very similar to that observed in the white hydrate material at Barkley Canyon. We suggest that hydrate growth from localized pockets of isolated gas can result in sI formation following the depletion of sII-forming gases within these individual hydrate reactors. Furthermore, thermodynamic modeling shows that for different initial gas compositions or *P*, *T* conditions, the same mechanism could result in other mixtures such sII–sH (e.g. Barkley Canyon 'yellow' hydrate) or sII–sH–sI hydrate (not yet observed in nature). The formation of hydrates from a multi-component gas led to a complex spatial distribution in structure and composition. This needs to be considered when evaluating how hydrate will respond to changes in its environment, such as pressure and temperature.

Acknowledgements

This work was supported through NURP grant UAF03-0098 and DOE grant DE-FC26-00NT4092. DORISS and PUP development was funded by a grant to MBARI from the David and Lucile Packard Foundation. Thanks to our Canadian colleagues (R. Chapman) for site navigation data, and for marking the sites.

Many thanks to the captains and crews of the R/V Point Lobos and Western Flyer and pilots of the ROV Ventana and Tiburon.

References

[1] E.D. Sloan, Clathrate Hydrates of Natural Gases, 2nd ed., Marcel Dekker, New York, USA, 1998.
[2] S. Subramanian, R. Kini, S. Dec, E.D. Sloan, Chem. Eng. Sci. 55 (1999) 1981.
[3] A.M. Trehu, C. Ruppel, M. Holland, G.R. Dickens, M.E. Torres, T.S. Collett, D. Goldberg, M. Riedel, P. Schultheiss, Oceanography 19 (4) (2006) 124–142.
[4] A.V. Milkov, Earth Sci. Rev. 66 (2004) 193–197.
[5] J.B. Klauda, S.I. Sandler, Energy Fuels 19 (2005) 459–470.
[6] G. Dickens, Geochem. Geophys. Geosyst. 2 (2001) (art. no. 2000GC000131).
[7] A.V. Milkov, G.E. Claypool, Y.-J. Lee, G.R. Dickens, W. Xu, W.S. Borowski, The ODP Leg 204 Scientific Party, Geology 31 (2003) 833–836.
[8] A.V. Milkov, Org. Geochem. 36 (5) (2005) 681–702.
[9] C.K. Paull, P.G. Brewer, W. Ussler III, E.T. Peltzer, G. Rehder, D. Clague, Geo. Mar. Lett. 22 (2003) 198–203.
[10] A.V. Milkov, G.E. Claypool, Y. Lee, R. Sassen, Geochim. Cosmochim. Acta 69 (4) (2005) 1007–1026.
[11] M. Kida, O. Khlystov, T. Zemskaya, N. Takahashi, H. Minami, H. Sakagami, A. Krylov, A. Hachikubo, S. Yamashita, H. Shoji, J. Poort, L. Naudts, Geophys. Res. Lett. 33 (2006) L24603.
[12] J. Brooks, M. Kennicutt, R. Fay, T. McDonald, R. Sassen, Science 225 (1984) 409–411.
[13] G.D. Ginsburg, V.A. Soloviev, Submarine gas hydrates, in: VNII Okeangeologia, St. Petersburg, 1998.
[14] J.W. Pohlman, E.A. Canuel, N.R. Chapman, G.D. Spence, M.J. Whiticar, R.D. Coffin, Org. Geochem. 36 (2005) 703–716.
[15] H. Lu, Y. Seo, J. Lee, I. Moudrakovski, J.A. Ripmeester, N.R. Chapman, R.B. Coffin, G. Gardner, J. Pojlman, Nature 445 (2007) 303–306.
[16] R. Sassen, H.H. Roberts, R. Carney, A.V. Milkov, D.A. DeFreitas, B. Lanoil, C. Zhang, Chem. Geol. 205 (2004) 195–217.
[17] T. Uchida, M. Moriwaki, S. Takeya, I.Y. Ikeda, R. Ohmura, J. Nagao, H. Minagawa, T. Ebinuma, H. Narita, K. Gohara, S. Mae, AIChE J. 50 (2) (2004) 518–523.
[18] D.F. Chen, L.M. Cathles, J. Geophys. Res. 108 (B1) (2003) 2058.
[19] P.G. Brewer, F.M. Orr, G. Friederich, K.A. Kvenvolden, D.L. Orange, J. McFarlane, W. Kirkwood, Geology 25 (5) (1997) 407–410.
[20] K.C. Hester, S.N. White, E.T. Peltzer, P.G. Brewer, E.D. Sloan, Mar. Chem. 98 (2006) 304–314.
[21] K.C. Hester, R.M. Dunk, S.N. White, P.G. Brewer, E.T. Peltzer, E.D. Sloan, Geochim. Cosmochim. Acta 7 (2007) 2947–2959.
[22] G. Rehder, S.H. Kirby, W.B. Durham, L.A. Stern, E.T. Peltzer, J. Pinkston, P.G. Brewer, Dissolution rates of pure methane hydrate and carbon-dioxide hydrate in undersaturated seawater at 1000-m depth 68 (2) (2004) 285–292.
[23] R.M. Dunk, E.T. Peltzer, P.M. Walz, P.G. Brewer, Environ. Sci. Technol. 39 (24) (2005) 9630–9636.
[24] S.N. White, R.M. Dunk, E.T. Peltzer, J.J. Freeman, P.G. Brewer, Geochem. Geophys. Geosyst. 7 (2006) Q05023.
[25] J.D. Pasteris, B. Wopenka, J.J. Freeman, P.G. Brewer, S.N. White, E.T. Peltzer, G. Malby, Appl. Spectrosc. 58 (7) (2004) 195A–208A.
[26] P. Brewer, G. Malby, J. Pasteris, S. White, E. Peltzer, B. Wopenka, J. Freeman, M. Brown, Deep Sea Res. 51 (2004) 739–753.
[27] S.N. White, W.J. Kirkwood, A.D. Sherman, M.O. Brown, R. Henthorn, K.A. Salamy, P.M. Walz, E.T. Peltzer, P.G. Brewer, Deep Sea Res. I 52 (12) (2005) 2376–2386.
[28] M. Haeckel, E. Suess, K. Wallmann, D. Rickert, Geochim. Cosmochim. Acta 68 (21) (2004) 4335–4345.
[29] E. Suess, M.E. Torres, G. Bohrmann, R.W. Collier, D. Rickert, C. Goldfinger, P. Linke, A. Heuser, H. Sahling, K. Heeschen, C. Jung, K. Nakamura, J. Greinert, O. Pfannkuche, A. Trehu, G. Klinkhammer, M.J. Whiticar, A. Eisenhauer, B. Teichert, M. Elvert, Sea floor methane hydrates at Hydrate Ridge, Cascadia Margin, in: C.K. Paull, W.P. Dillion (Eds.), Natural Gas Hydrates: Occurrence, Distribution and Detection, American Geophysical Union, Washington, DC, 2001, pp. 87–98.
[30] G. Rehder, P. Brewer, E.T. Peltzer, G. Friederich, Geophys. Res. Lett. 29 (15) (2002) 1731.
[31] A.K. Sum, R.C. Burruss, E.D. Sloan, J. Phys. Chem. B 101 (38) (1997) 7371–7377.
[32] K.C. Hester, Probing hydrate stability and structural characterization of both natural and synthetic clathrate hydrates, in: Ph.D. Chemical Engineering, Colorado School of Mines, Golden, United States of America, 2007.
[33] S. Subramanian, E.D. Sloan, J. Phys. Chem. B 106 (17) (2002) 4348–4355.
[34] S.R. Davies, M.S. Selim, E.D. Sloan, P. Bollavaram, D.J. Peters, AIChE J. 52 (12) (2006) 4016–4027.
[35] A.L. Ballard, E.D. Sloan, Fluid Phase Equilibr. 194-197 (2002) 371–383.
[36] G.D. Spence, N.R. Chapman, R.D. Hyndman, C. Cleary, EOS Trans. AGU 82 (50) (2001) 621.
[37] R. Chapman, J. Pohlman, R. Coffin, J. Chanton, L. Lapham, EOS 85 (38) (2004) 361–368.
[38] S. Takeya, Y. Kamata, T. Uchida, J. Nagao, T. Ebinuma, H. Narita, A. Hori, T. Hondoh, Can. J. Phys. 81 (2003) 479–484.
[39] S. Subramanian, A. Ballard, R.A. Kini, S. Dec, E. Sloan, Chem. Eng. Sci. 55 (2000) 5763–5771.
[40] R. Sassen, S. Sweet, D. DeFreitas, A. Milkov, Org. Geochem. 31 (2000) 1257.
[41] R.M. Dunk, 2007, unpublished data.
[42] S.A. Burikov, I.V. Churina, S.A. Dolenko, T.A. Dolenko, V.V. Fadeev, EARSeL eProceedings, 2004, pp. 298–305.
[43] R. Sassen, I.R. MacDonald, Org. Geochem. 22 (6) (1994) 1029–1032.